Supplemental Information: Combined simulation and experimental study of large deformation of red blood cells in microfluidic systems

David J. Quinn, Igor V. Pivkin, Sophie Wong, Keng-Hwee Chiam, Ming Dao, George Karniadakis, Subra Suresh

November 4, 2010

1   Governing Equations for RBC and DPD Models

The membrane model consists of points $\{\mathbf{r}_n, n \in 1..N\}$ which are the vertices of surface triangulation (Figure S1). The area of triangle $\alpha \in 1..\Pi$ formed by vertices (l, m, n) is given by $A_\alpha = |(\mathbf{r}_m - \mathbf{r}_l) \times (\mathbf{r}_n - \mathbf{r}_l)|/2$. The length of the link $i \in 1..S$ connecting vertices m and n is given by $L_i = |\mathbf{r}_m - \mathbf{r}_n|$. The in-plane free energy of the membrane

$$F_{\text{in-plane}} = \sum_{i \in \text{links}} V_{\text{WLC}}(L_i) + \sum_{\alpha \in \text{triangles}} C/A_\alpha, \tag{1}$$

includes the worm-like chain (WLC) potential for individual links

$$V_{WLC}(L) = \frac{k_B T L_{\max}}{4p} \times \frac{3x^2 - 2x^3}{1 - x}, \tag{2}$$

where $x = L/L_{\max} \in (0, 1)$, $L_{\max}$ is the maximum length of the links and p is the persistence length; the parameter C in the hydrostatic elastic energy term is defined as in (1). The
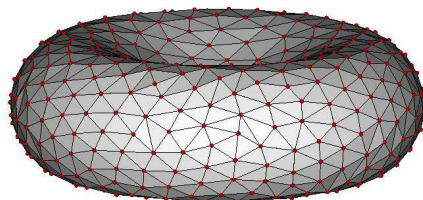
Figure S1: Coarse-grained RBC, represented by collection of points connected by links. The model takes into account the effects of membrane viscosity, in-plane shear energy, bending energy, constraints of fixed surface area and enclosed volume.

bending energy is given by

$$F_{\text{bending}} = \sum_{\text{adjacent } \alpha, \beta \text{ pair}} k_{\text{bend}}[1 - cos(\theta_{\alpha\beta} - \theta_0)], \tag{3}$$

where k_{bend} is the average bending modulus (2), while θ_0 and $\theta_{\alpha\beta}$ are the spontaneous and the instantaneous angles between two adjacent triangles, respectively. The total volume and surface area constraints are given by

$$F_{\text{volume}} = \frac{k_{\text{volume}}(\Omega - \Omega_0)^2 k_B T}{2L_0^3 \Omega_0}, \tag{4}$$

and

$$F_{\text{surface}} = \frac{k_{\text{surface}}(A - A_0)^2 k_B T}{2L_0^2 A_0}, \tag{5}$$

respectively, where L_0 is the average length of the link, Ω and Ω_0 are the instantaneous and equilibrium volumes of the model, and A and A_0 are instantaneous and equilibrium surface areas. The parameters k_{volume} and k_{surface} are adaptively adjusted during the simulations to keep the deviations of instantaneous volume and surface area from the equilibrium values to less than 1%. The elastic contribution to the forces on point $n \in 1..N$ is obtained as

$$\mathbf{f}_n^E = -\partial(F_{\text{in-plane}} + F_{\text{bending}} + F_{\text{volume}} + F_{\text{surface}})/\partial\mathbf{r}_n. \tag{6}$$

The effect of membrane viscosity is modeled by adding frictional resistance to each link. The viscous contribution to the force on point $n \in 1..N$ is given by

$$\mathbf{f}_n^V = -\sum_{(n,m)\in\text{links}} \gamma_{\text{RBC}}(\mathbf{v}_{nm} \cdot \hat{\mathbf{r}}_{nm})\mathbf{r}_{nm}, \tag{7}$$

where $\mathbf{v}_{nm} = \mathbf{v}_m - \mathbf{v}_n$, $\mathbf{r}_{nm} = \mathbf{r}_m - \mathbf{r}_n$, $r_{nm} = |\mathbf{r}_{nm}|$, $\hat{\mathbf{r}}_{nm} = \mathbf{r}_{nm}/r_{nm}$, and $\mathbf{v}_n$ is the velocity of point n.

In simulations surrounding fluid and RBC internal fluid (hemoglobin) are modeled using Dissipative Particle Dynamics (3, 4). All particles are assumed to have the same mass equal to $M = 1$ in simulations. The particles interact with each other through conservative, dissipative and random force. Specifically, the forces exerted on a particle n by particle m are given by

$$\mathbf{f}_{nm}^C = f^C(r_{nm})\hat{\mathbf{r}}_{nm}, \tag{8}$$
$$\mathbf{f}_{nm}^D = -\gamma w^D(r_{nm})(\hat{\mathbf{r}}_{nm} \cdot \mathbf{v}_{nm})\hat{\mathbf{r}}_{nm}, \tag{9}$$
$$\mathbf{f}_{nm}^R = \sigma w^R(r_{nm})\xi_{nm}\hat{\mathbf{r}}_{nm}. \tag{10}$$

The parameters γ and σ determine the strength of the dissipative and random forces, respectively. Also, ξ_{nm} are symmetric Gaussian random variables with zero mean and unit variance, and are independent for different pairs of particles and at different times; $\xi_{nm} = \xi_{mn}$ is enforced in order to satisfy momentum conservation. Finally, ω^D and ω^R are weight functions.

All forces act within a sphere of interaction radius r_c, which is the length scale of the system. The conservative force is given by

$$\mathbf{f}_{nm}^C = \begin{cases} a(1 - r_{nm}/r_c)\hat{\mathbf{r}}_{nm}, & r_{nm} < r_c \\ 0, & r_{nm} \geq r_c \end{cases}, \tag{11}$$

where a is a conservative force coefficient. The requirement of the canonical distribution sets two conditions on the weight functions and the amplitudes of the dissipative and random forces (3, 5)

$$\omega^D(r_{nm}) = \left[\omega^R(r_{nm})\right]^2, \tag{12}$$

and

$$\sigma^2 = 2\gamma k_B T_{\text{DPD}}, \tag{13}$$

where T_{DPD} is the DPD system temperature and k_B is the Boltzmann constant. The weight function takes the form (6)

$$\omega^D(r_{nm}) = [\omega^R(r_{nm})]^2 = \begin{cases} (1 - r_{nm}/r_c)^s, & r_{nm} \leq r_c, \\ 0, & r_{nm} > r_c, \end{cases} \tag{14}$$

with exponent $s \leq 2$ ($s = 2$ for standard DPD). The value of exponent s affects the viscosity of the DPD fluid for fixed parameters σ and γ in dissipative and random forces. Lower values of s typically result in a higher viscosity of the fluid. Larger values of dissipative force coefficient γ increase the viscosity of the DPD fluid but lower the temperature of the DPD fluid. In all cases we have verified that there are no solidification artifacts associated with lower temperatures. This was done by calculating the radial distribution function as well as diffusion coefficient of the DPD fluid. In addition, the Newtonian behavior of the DPD fluid was verified using Poiseuille flow with known exact solution.

When the RBC model is immersed into the DPD fluid, each particle experiences membrane elastic and viscous forces in addition to the DPD forces from the surrounding fluid particles. Therefore, the total force exerted on a membrane particle is given by

$$\mathbf{f}_n = \mathbf{f}_n^E + \mathbf{f}_n^V + \mathbf{f}_n^C + \mathbf{f}_n^D + dt^{-1/2}\mathbf{f}_n^R, \tag{15}$$

while for a fluid particle

$$\mathbf{f}_n = \mathbf{f}_n^C + \mathbf{f}_n^D + dt^{-1/2}\mathbf{f}_n^R. \tag{16}$$

Here $\mathbf{f}_n^C = \sum_{n \neq m} \mathbf{f}_{nm}^C$ is the total conservative force acting on particle n; $\mathbf{f}_n^D$ and $\mathbf{f}_n^R$ are defined similarly. The $dt^{-1/2}$ term multiplying random force $\mathbf{f}_n^R$ in equations (15) and (16) is there to ensure that the diffusion coefficient of the particles is independent of the value of the timestep dt used in simulations (3). The time evolution of the particles is described by Newton's law

$$d\mathbf{r}_n = \mathbf{v}_n dt, \tag{17}$$

$$d\mathbf{v}_n = \frac{1}{M}\mathbf{f}_n dt. \tag{18}$$

The simulations are done in non-dimensional units and therefore it is necessary to establish the link between DPD and physical scales. Specifically, we need to define the DPD units of length, time and energy.

The unit of length (the DPD cutoff radius r_c) in simulations is equal to 1 micron. The equilibrium, persistence and maximum length of the links, as well as other parameters of RBC model are set according to (7). In addition, we use two independent experimental measurements to specify the units of energy and time in DPD. Specifically, we require that

the amplitude of thermal fluctuations of the membrane at rest are within the range of experimentally observed (8). The amplitude of the membrane thermal fluctuations is affected mostly by the choice of DPD unit of energy in simulations. We also require that the characteristic relaxation time of the RBC model in simulations is equal to experimentally measured value of 0.16s at room temperature. The relaxation time is affected mostly by the ratio of membrane elastic and viscous forces. In simulations corresponding to 37C and 41C, the membrane viscosity is decreased by 50 and 63.5 per cent, respectively, to match experimentally measured relaxation time at these temperatures. The rest of the simulation parameters are based on these units of length, time and energy.

The fluid domain in simulations corresponds to the middle part of the microfluidic device. The width of the flow domain is $60\mu m$, the length is $200\mu m$, the height is $2.7\mu m$. The central part of the simulation domain is the same as in the experiment. Specifically, the flow is constricted to rectangular cross-section of 4, 5 or 6 μm in width and $2.7\mu m$ in height. The walls are modeled by freezing DPD particles in combination with bounce-back reflection, similar to (9). The flow is sustained by applying an external body force. The passage of the RBC through the microchannel with the dimension smaller than the size of the resting RBC involves large deformations of the cell followed by the recovery of the biconcave shape. Therefore, the ratio of the characteristic relaxation time and the RBC transition time is the same in our simulations as in the microfluidic experiments. A single experimental data point (4 μm wide x 2.7 μm high channel, 44 Pa pressure difference, room temperature) is used to estimate this ratio. The unit of the DPD external body force is then calculated to match this ratio and later used to model the remaining experimental conditions.

Previous theoretical analysis revealed that the resting RBC biconcave shape is defined by the membrane bending energy and constraints of surface area and total volume of the RBC (10, 11). The elastic shear energy at equilibrium is likely to be at the minimum due to the reorganization of the spectrin network (12). The process of spectrin reorganization seems to be quite slow with characteristic time of the order of seconds, while the characteristic time of deformations in our experiments is of the order of 10^{-2} seconds (13–15). Therefore, the material reference state for the in-plane elastic energy of the model is chosen to be a biconcave shape (7) and spectrin network reorganization is not considered in our simulations. As discussed in the main text, this latter assumption may not be valid for the smallest cross-section used in the experiments (i.e. 2.7 μm x 3 μm).

2 Measurement of local pressure difference across microfluidic channels

Across several experimental runs, differences in hydrodynamic pressure losses may arise due to several factors, such as minor leaks, the presence of debris in the channel reservoirs, and cell concentration gradients. Such variability would result in differences in cell traversal/flow behavior under the same nominally applied upstream/downstream pressure differences. Therefore, in order to minimize the effect of these variations as well as minimize the physical domain required in our DPD simulations, a particle tracking scheme was used to experimentally determine the local pressure gradients in the microfluidic channel.

Viscous flow of a Newtonian fluid with viscosity (η) through a channel of rectangular cross-section with width (w), height (h) and length (L) may be described by the well-known pressure-velocity relationship (16):

$$V(x,y) = \frac{\Delta P}{\eta L} \frac{4h^2}{\pi^3} \sum_{n=1,3,5,\ldots}^{\infty} \frac{1}{n^3} \left(1 - \frac{\cosh(n\pi x/h)}{\cosh(n\pi w/2h)}\right) \sin(n\pi y/h) \tag{19}$$

where $-w/2 \leq x \leq w/2$ and $0 \leq y \leq h$. Neutrally-buoyant, rigid particles with a diameter (D_p) that is small compared to the length and width of the channel ($D_p << w$ and $D_p << h$) may be expected to flow along streamlines and give a direct measurement of the fluid velocity at a point corresponding to the center of the particle. Thus, a measured average fluid velocity may be used to infer a pressure difference from an integrated/averaged form of Equation 19. However, due to imaging limitations and the small channel dimensions used in this work, we are required to use minimum particle diameters of $1\mu m$, which is comparable to both the channel height and width. In this case, the particle may be expected to travel with a velocity comparable to the average fluid velocity over the projected area of the particle. In addition, the particle may not perfectly track the fluid streamlines due to rotational effects brought upon by the high velocity gradients in the length or width direction. Therefore, in order to establish a relationship between the measured bead trajectories and the local pressure gradient, a combination of numerical averaging and computational fluid dynamics studies (CFD) was used. First, it is important to realize that bead trajectories are limited to the region: $-w/2 + D_p/2 \leq x \leq w/2 - D_p/2$ and $D_p/2 \leq y \leq h - D_p/2$. Over this region, a grid of points with coordinates (x_b, y_b) and separation $(\delta x, \delta y)$ may be selected for which the velocity of the beads at those points may be approximated by the average fluid velocity of the circular region of radius $R_p = D_p/2$ around that point. These bead velocities may be averaged over the bead flow region to establish a relationship between the average bead velocity and the local pressure difference. This relationship is plotted for the channels and temperatures used in our experiments in Figure S2. In calculating these relationships, the fluid is assumed to have the same temperature-dependent viscous properties as water (17–19). This relationship was compared to the results of a series of CFD simulations of a flow of 1 μm particles in a 2.7 μm high x 4 μm wide channel. These CFD results indicated that for flow off the centerline of the channel, rotational effects are present and beads do not exactly travel along the fluid streamlines. However, as shown in Figure S3, these effects have only a small effect on the bead's average velocity in the microfluidic channel compared to that calculated using the local average of 19. Therefore, the relationships presented in Figure S2 are believed to be adequate for inferring the local pressure gradient for a measured average bead velocity.

In our experiments, the minimum depth of field of our imaging system was estimated to be 2.8 μm using the analysis presented in (20). Thus, bead images are believed to be taken along the entire channel height. These bead trajectories were tracked and subsequently analyzed using an image segmentation and tracking routine written in Matlab. Average velocity measurements were checked by manually tracking a subset of beads from every data-set. The average bead velocity is then translated to a local pressure differential using the relationships presented in Figure S2.
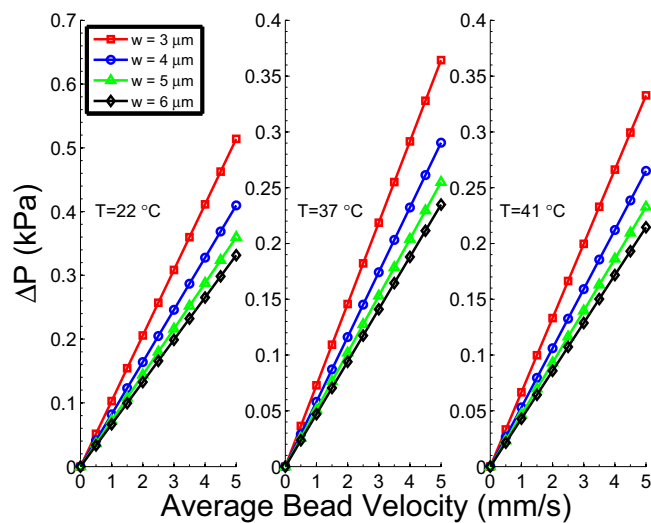
Figure S2: Relationship between average velocities of $1\mu m$ diameter beads and local pressure difference at room, body and febrile temperatures (22°C, 37°C and 41°C, respectively) for 2.7 μm high, 30 μm long channels of varying width.
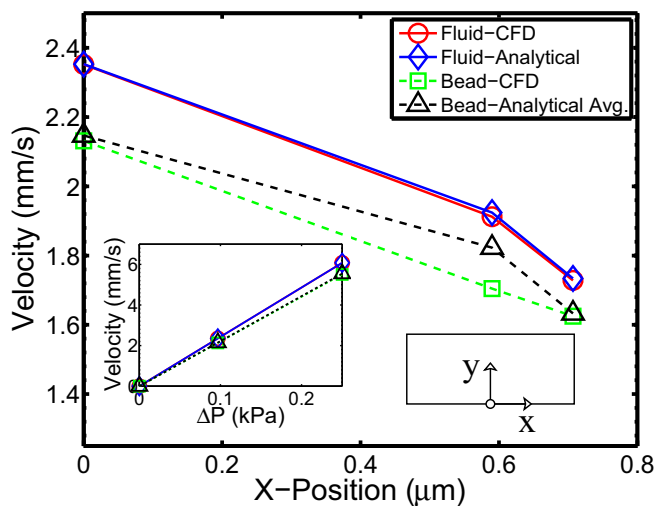
Figure S3: Comparison of analytical solutions and CFD results for fluid and bead velocities at various positions along the width of the channel. (Inset: Pressure-velocity relationship for beads and fluid along channel center-line)

References

1. Boey, S. K., D. H. Boal, and D. E. Discher, 1998. Simulations of the erythrocyte cytoskeleton at large deformation. I. Microscopic models. *Biophys J* 75:1573–1583.

2. Boal, D. H., and M. Rao, 1992. Topology changes in fluid membranes. *Phys Rev A* 46:3037–3045.

3. Groot, R. D., and P. B. Warren, 1997. Dissipative particle dynamics: Bridging the gap between atomistic and mesoscopic simulation. *J Chem Phys* 107:4423–4435.

4. Hoogerbrugge, P. J., and J. M. V. A. Koelman, 1992. Simulating microscopic hydrodynamic phenomena with dissipative particle dynamics. *Europhys Lett* 19:155–160.

5. Espanol, P., and P. Warren, 1995. Statistical mechanics of dissipative particle dynamics. *Europhys Lett* 30:191–196.

6. Fan, X., N. Phan-Thien, S. Chen, X. Wu, and T. Y. Ng, 2006. Simulating flow of DNA suspension using dissipative particle dynamics. *Phys Fluids* 18:63102–63110.

7. Pivkin, I. V., and G. E. Karniadakis, 2008. Accurate coarse-grained modeling of red blood cells. *Phys Rev Lett* 101:118105.

8. Park, Y., M. Diez-Silva, G. Popescu, G. Lykotrafitis, W. Choi, M. S. Feld, and S. Suresh, 2008. Refractive index maps and membrane dynamics of human red blood cells parasitized by Plasmodium falciparum. *Proc Natl Acad Sci USA* 105:13730–13735.

9. Pivkin, I. V., and G. E. Karniadakis, 2005. A new method to impose no-slip boundary conditions in dissipative particle dynamics. *J Comput Phys* 207:114–128.

10. Canham, P. B., 1970. The minimum energy of bending as a possible explanation of the biconcave shape of the human red blood cell. *J Theor Biol* 26:61–81.

11. Helfrich, W., 1973. Elastic properties of lipid bilayers: theory and possible experiments. *Z Naturforsch* 28:693–703.

12. Deuling, H. J., and W. Helfrich, 1976. Red blood cell shapes as explained on the basis of curvature elasticity. *Biophys J* 16:861–868.

13. Mills, J. P., L. Qie, M. Dao, C. T. Lim, and S. Suresh, 2004. Nonlinear elastic and viscoelastic deformation of the human red blood cell with optical tweezers. *MCB* 1:169–180.

14. Evans, E. A., and R. M. Hochmuth, 1976. Membrane viscoelasticity. *Biophys J* 16:1–11.

15. Hochmuth, R. M., P. R. Worthy, and E. A. Evans, 1979. Red-cell extensional recovery and the determination ofmembrane viscosity. *Biophys J* 26:101–114.

16. Mortensen, N., F. Okkels, and H. Bruus, 2005. Reexamination of Hagen-Poiseuille flow: Shape dependence of the hydraulic resistance in microchannels. *Phys Rev E* 71:57301–57304.

17. Wetzel, R., M. Becker, J. Behlke, H. Billwitz, S. Böhm, B. Ebert, H. Hamann, J. Krumbiegel, and G. Lassmann, 1980. Temperature behaviour of human serum albumin. *Eur J Biochem* 104:469–478.

18. Neurath, H., G. R. Cooper, and J. O. Erickson, 1941. The shape of protein molecules II. Viscosity and diffusion studies of native proteins. *J Biol Chem* 138:411–436.

19. Chatterjee, A., 1965. Intrinsic viscosity measurements of bovine serum albumin at different temperatures. *Nature* 205:386.

20. Meinhart, C. D., S. T. Wereley, and M. H. B. Gray, 2000. Volume illumination for two-dimensional particle image velocimetry. *Meas Sci Technol* 11:809–814.